processes

Article

Bidirectional Resonant Converter for DC Microgrid Applications

Bor-Ren Lin

Department of Electrical Engineering, National Yunlin University of Science and Technology, Yunlin 640, Taiwan; linbr@yuntech.edu.tw

Abstract: A bidirectional resonant converter is presented and verified in this paper for an electric vehicle battery charger/discharger system. The presented circuit can achieve forward and backward power operation, low switching losses on active devices, and wide output voltage operation. The circuit structure of the presented converter includes two resonant circuits on the primary and secondary sides of an isolated transformer. The frequency modulation approach is adopted to control the studied circuit. Owing to the resonant circuit characteristic, active devices for both forward (battery charge) and backward (battery discharge) power operation can be turned on at zero voltage switching. In order to implement a universal battery charger for different kinds of electric vehicle applications, the DC converter is demanded to have a wide output voltage range capability. The topology morphing between a full bridge resonant circuit and half bridge resonant circuit is selected to obtain high- and low-output voltage range operations so that the 200–500 V output voltage range is realized in the presented resonant converter. Compared to the conventional bidirectional converters, the proposed can be operated under a wide voltage range operation. In the end, a 1 kW laboratory prototype circuit is built, and experiments are provided to demonstrate the validity and performance of the presented bidirectional resonant converter.

Keywords: resonant converter; bidirectional power operation; DC microgrid

Citation: Lin, B.-R. Bidirectional Resonant Converter for DC Microgrid Applications. *Processes* **2021**, *9*, 1664. https://doi.org/10.3390/pr9091664

Academic Editors: Chang-Hua Lin

Received: 6 August 2021
Accepted: 13 September 2021
Published: 15 September 2021

1. Introduction

For the development of renewable energy, the DC microgrid or nanogrid systems have been widely studied to support one of local power distribution networks. The DC/DC converters or AC/DC converters [1–5] are demanded to convert unstable DC voltage from solar power or fuel cell power or unstable AC voltage from wind power into a stable DC bus voltage. Then, the DC bus voltage on the DC microgrid can supply power to residential houses, commercial buildings, and industry factories. Normally, DC/DC converters or DC/AC converters are needed to convert the DC bus voltage into low DC voltage for commercial or personal power units or AC voltage for motor drives. In order to reduce oil demand and air pollution, electric vehicles have been widely developed in recent years with using battery packs instead of gasoline as their power source. Therefore, the bidirectional AC/DC or DC/DC converters are demanded [6–8] to achieve battery charge and discharge. In [9,10], the phase-shift pulse-width modulation (PWM) converter has been proposed to achieve buck/boost operation under forward/backward power flow operation. However, this circuit topology has high circulating current loss at freewheeling state and low circuit efficiency at low duty cycle operation if the wide voltage range is demanded. In [11–14], dual active bridge (DAB) PWM converters have been developed and implemented to have bidirectional power operation with V_o = 300–450 V voltage range. The phase shift technique and duty cycle control are used in DAB converters to control power flow between input and output terminals. However, the phase angle between two terminals and duty cycle PWM signals are more complicated to calculate and derived compared to these other bidirectional power converters. In [15,16], the symmetric resonant converters have been studied and achieved to realize bidirectional power operation using the frequency modulation approach. Therefore, the active devices can be turned on at zero voltage switching. However, the input or output voltage of this circuit topology is limited at a finite range such as 400–600 V input or 300–450 V output voltage range. The advantage of the resonant converter is the low switching loss on active devices and has been discussed in [15,16]. However, the symmetric resonant converter cannot achieve well if the wide voltage range operation is demanded for universal battery charge/discharge circuit.

A bidirectional DC/DC converter is presented to have low switching loss on active devices, forward/backward power operation, and wide voltage operation for battery charge/discharge applications on a DC microgrid system. The input voltage of the presented converter is from DC bus voltage on DC microgrid system. For forward power operation, power flow is from DC microgrid to battery. For backward power operation, power flows is from battery to DC microgrid. Two full bridge resonant circuits are used in the studied converter to achieve bidirectional power flow capability. The power flow and voltage regulation are controlled by using a frequency modulation approach. The adopted resonant circuit has a soft switching characteristic for all power switches. Thus, the switching loss on active devices is reduced. The variable half/full bridge resonant circuit structure is used in the presented converter to solve limit voltage gain disadvantage on conventional bidirectional resonant converters. When low voltage output is requested, the half bridge resonant circuit is operated to achieve low voltage gain. If the high output is demanded in the proposed converter, full bridge resonant circuit is operated to realize high voltage gain. Thus, a wide output voltage operation is implemented in the studied circuit. The presented bidirectional DC/DC converter can be applied to a universal battery charge/discharge system in electric vehicle systems or battery charge stations. The circuit schematic is presented in Section 2. The operation of principle is discussed in Section 3. The circuit analysis and design example are provided in Section 4. Experiments are provided in Section 5 to verify the performance of the proposed converter. In Section 6, a conclusion of the studied DC converter is provided.

2. Circuit Schematic of the Presented Converter

Figure 1 shows the block diagrams of the simplified DC nanogrid or microgrid system. Normally, the DC microgrid inputs can be DC power (solar power, fuel cell power, or HVDC transmission supply) or AC power (AC transmission supply or wind power). The microgrid outputs may be AC loads (motor drives), DC loads (personal computers or server systems), or battery stacks in electric vehicle applications. For residential house or industry factory applications, the bus voltage of DC microgrid system is normally controlled at 380 V. For modern battery charger/discharger system in electric vehicle applications, the bidirectional DC/DC converter is demanded to achieve grid-to-vehicle (G2V) and vehicle-to-grid (V2G) power flow operations. The conventional buck/boost converter shown in Figure 2a is used to realize forward and backward power flows for battery charge and discharge operations. However, no electric isolation is given in bidirectional buck/boost converter. Figure 2b gives the circuit diagram of a dual active bridge converter to achieve bidirectional power operation. By controlling the phase-angle between the leg voltages V_{ab} and V_{cd}, the forward or backward power can be regulated and controlled between input and output terminals. However, dual active bridge converter has the circulating current losses at the freewheeling state. Figure 2c gives the circuit diagram of a dual resonant converter to realize bidirectional power flow operations. The symmetric resonant circuits are adopted on the primary and secondary sides so that the converter operated at forward power and backward power operations has similar circuit characteristics. The advantages of the resonant converters [17,18] are low switching losses on power devices and low electromagnetic interference. However, the dual resonant converter has less voltage gain so that the available input or output voltage is limited at a finite range.

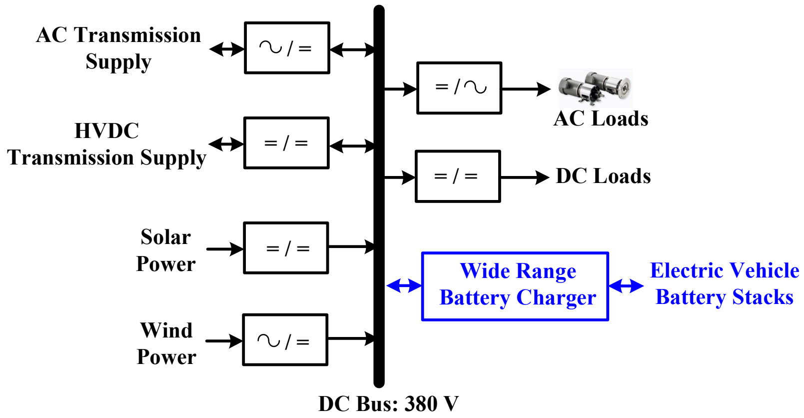

Figure 1. Block diagram of a simplified DC microgrid system.

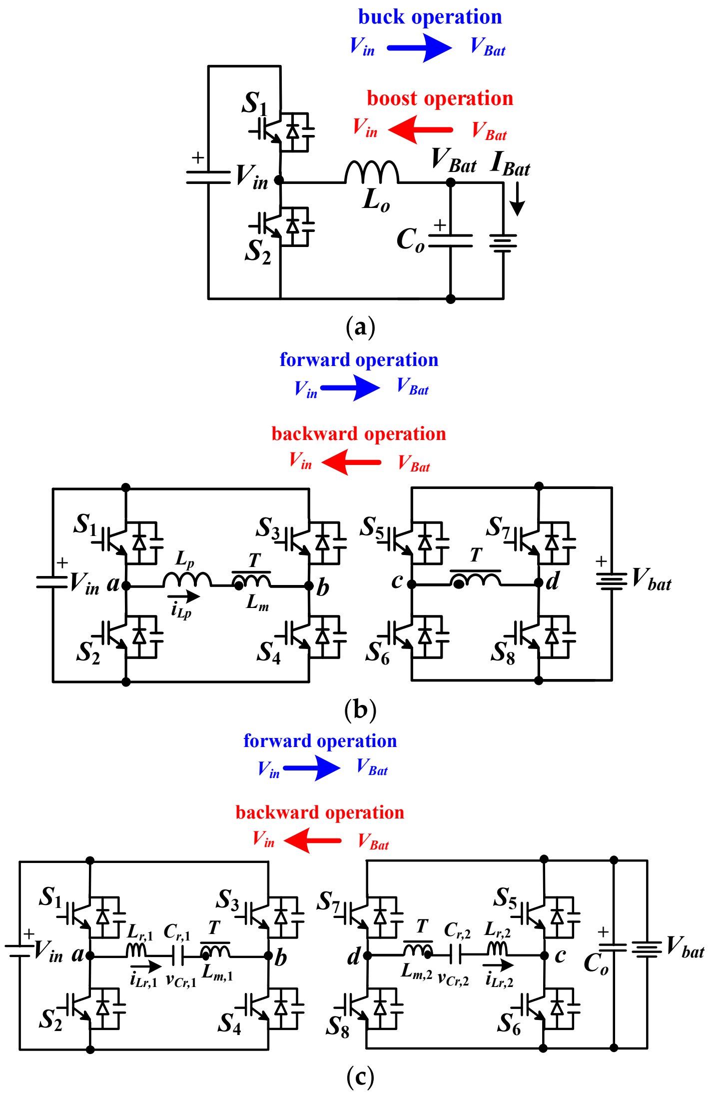

Figure 2. Circuit diagrams of bidirectional DC/DC converter: (**a**) buck/boost converter; (**b**) dual active bridge converter; (**c**) dual resonant converter.

The circuit schematic of the presented converter is shown in Figure 3a. Compared to the conventional dual resonant converter, the proposed converter has more wide output voltage range operation with bidirectional power flow operation and soft switching operation on all active devices. Full bridge circuit and one additional ac switch S_{ac} are adopted on the input voltage terminal. Similarly, the other full bridge circuit is adopted on the output voltage terminal in the proposed circuit. For forward power operation, S_5–S_8 are off so that the secondary side circuit is similar to a full bridge diode rectifier. When low-output voltage range is demanded to charge the battery stack, S_{ac} is on and S_3 and S_4 are off. Only S_1 and S_2 are controlled by the frequency modulation scheme. Figure 3b gives the equivalent circuit structure of the presented converter operated at low-output voltage range and forward power operation. One can observe that the equivalent circuit in Figure 3b is a half bridge resonant circuit. When high-output voltage range is requested to charge battery stack, S_{ac} is off and S_1–S_4 are controlled with frequency modulation scheme. The equivalent circuit of the presented converter operated at forward power operation and high-output voltage range is shown in Figure 3c. Basically, the circuit in Figure 3c is a full bridge resonant converter. Since the leg voltage V_{ab} in Figure 3c (full bridge resonant circuit) is two times that of the leg voltage V_{ac} in Figure 3b (half bridge resonant circuit), the presented converter has a larger output voltage under full bridge resonant structure (Figure 3c) than half bridge resonant structure (Figure 3b). For backward power operation, the switches S_5–S_8 are controlled with variable frequency modulation to transfer power from V_o side to V_{in}. Since the V_o is discharged from a high-voltage level, full bridge diode rectifier is adopted on the left hand side of the proposed circuit. Therefore, S_5–S_8 and S_{ac} are all off and the equivalent circuit under backward power operation is shown in Figure 3d.

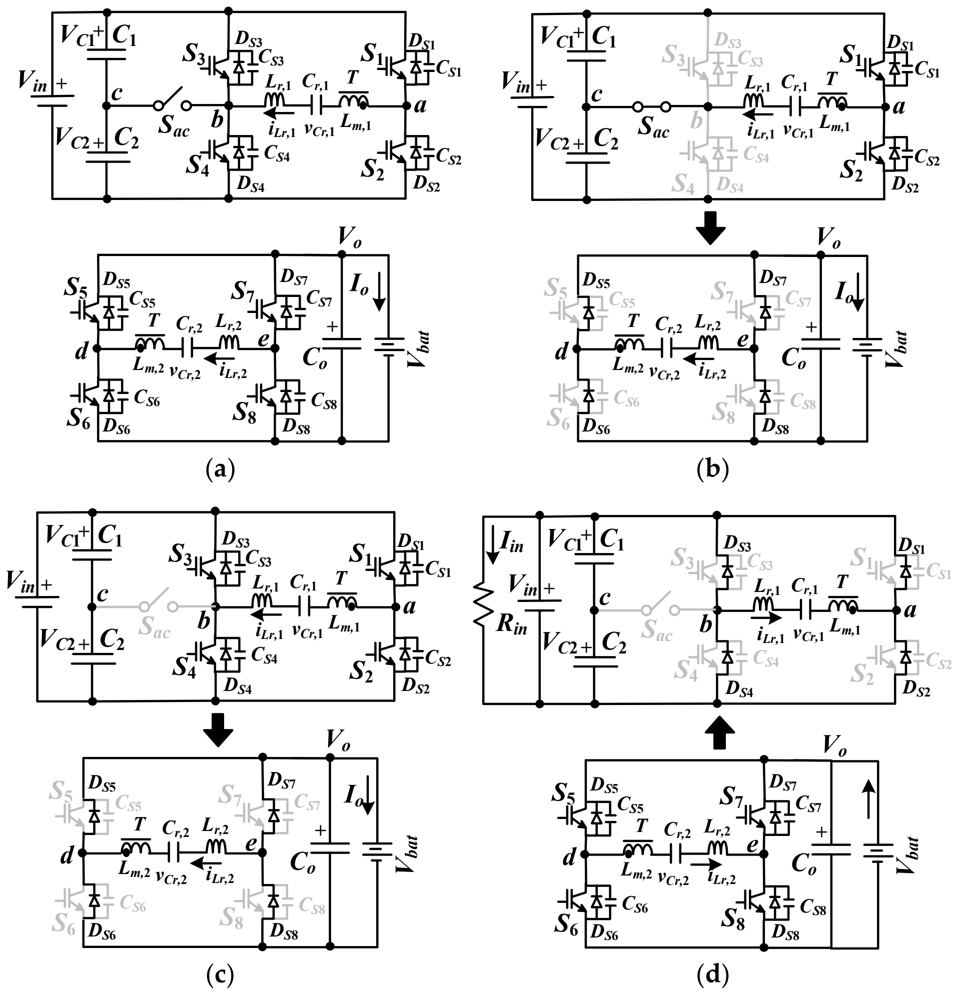

Figure 3. Proposed resonant converter with bidirectional power flow and wide output voltage operation: (**a**) circuit structure; (**b**) forward power flow and low output voltage range; (**c**) forward power flow and high-output voltage range; (**d**) backward power operation.

3. Principle of Operation

The presented circuit has three different operation modes as shown in Figure 3b–d to achieve bidirectional power operation and wide output voltage operation. Three operation modes are presented in the following discussions. Figure 4 gives the voltage and current waveforms for these three operation modes. For every switching cycle, there are eight operating states according to the conducting status of switches and diodes.

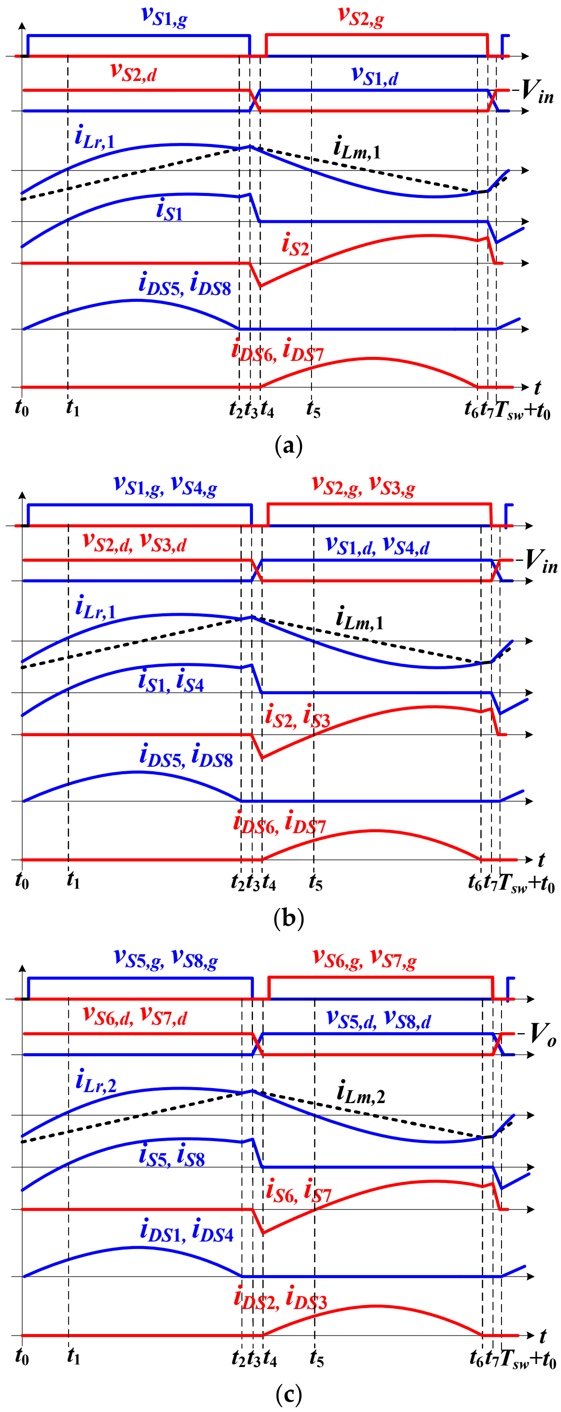

Figure 4. Main voltage and current waveforms of the proposed converter at (**a**) forward power operation and low-output voltage range; (**b**) forward power operation and high-output voltage range; (**c**) backward power operation.

3.1. Low-Output Voltage Range under Forward Power Operation

If the battery stack is at a low-voltage level, the proposed converter is needed to output low voltage. In order to achieve wide output voltage range operation, the half bridge resonant circuit as shown in Figure 3b is adopted to accomplish forward power operation. Switch S_{ac} is on and S_3, S_4 and S_5–S_8 are off. Only S_1 and S_2 are controlled with frequency modulation approach. The secondary side is similar to a full bridge diode rectifier. According to the status of active switches and diodes, eight switching states are observed in every switching cycle as shown in Figure 4a if $f_{sw} < f_r$ (resonant frequency). To simplify the circuit discussion, the circuit components are assumed as $C_{r,1} = C_{r,2}/n^2$ and $L_{r,1} = n^2L_{r,2}$ where $n = n_p/n_s$ so that the converter has same resonant frequency for both forward and backward power operations. Figure 5 gives the circuits of these eight switching states.

State 1 [t_0, t_1]: $v_{CS1} = 0$ at t_0. Since $i_{Lr,1}(t_0) < 0$, the anti-parallel diode D_{S1} conducts. Therefore, switch S_1 turns on at this moment to achieve zero voltage switching. The current $i_{Lr,2}$ increases and D_{S5} and D_{S8} are forward biased.
State 2 [t_1, t_2]: At t_1, $i_{Lr,1} > 0$ so that diode D_{S1} becomes off and $i_{Lr,1}$ flows through S_1 instead of D_{S1}. Power is transferred from V_{C1} to V_o in this state. The input and output leg voltages are $V_{ac} = V_{C1} = V_{in}/2$ and $V_{de} = V_o$. In this state, the resonant frequency is $f_r = 1/(2\pi\sqrt{L_{r,1}C_{r,1}})$.
State 3 [t_2, t_3]: If $f_{sw} < f_r$, $i_{Lr,2} = 0$ at t_2. Thus, D_{S5} and D_{S8} are off. Since $C_1 >> C_{r,1}$, the resonant frequency in state 3 is given as $f_p = 1/(2\pi\sqrt{C_{r,1}(L_{m,1} + L_{r,1})})$.
State 4 [t_3, t_4]: S_1 turns off at t_3. Then, $i_{Lr,1}$ will charge C_{S1} and discharge C_{S2}. If the current $i_{Lr,1}(t_3) = i_{Lm,1,peak} > V_{in}\sqrt{2C_{S,1}/L_{r,1}}$ where $C_{S,1} = C_{S1} = C_{S2} = C_{S3} = C_{S4}$ and $i_{Lm,1,peak}$ is the peak value of $i_{Lm,1}$, then C_{S2} can be discharged to zero voltage.
State 5 [t_4, t_5]: $v_{CS2} = 0$ at t_4. Since $i_{Lr,1}(t_4) > 0$, the anti-parallel diode D_{S2} conducts. Therefore, S_2 can be turned on at this moment to realize zero voltage switching. The current $i_{Lr,2}$ decreases so that D_{S6} and D_{S7} are conducting.
State 6 [t_5, t_6]: At t_5, $i_{Lr,1} < 0$ so that D_{S2} is off. $i_{Lr,1}$ flows through S_2. Power is transferred from V_{C2} to V_o in state 6. The resonant frequency in state 6 is $f_r = 1/(2\pi\sqrt{L_{r,1}C_{r,1}})$.
State 7 [t_6, t_7]: At time t_6, $i_{Lr,2} = 0$. Then, D_{S6} and D_{S7} become off. Since $C_2 >> C_{r,1}$, the resonant frequency in state 7 is $f_p = 1/(2\pi\sqrt{C_{r,1}(L_{m,1} + L_{r,1})})$.
State 8 [t_7, $T_{sw} + t_0$]: At time t_7, S_2 is turned off. Since $i_{Lr,1}(t_7) < 0$, C_{S1} (C_{S2}) is discharged (charged) in this state. This switching cycle is ended at time $T_{sw} + t_0$.

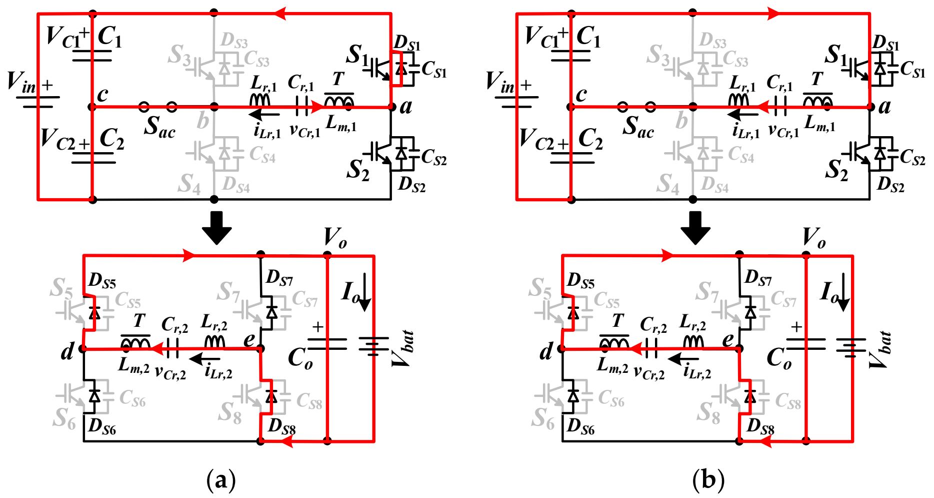

Figure 5. *Cont.*

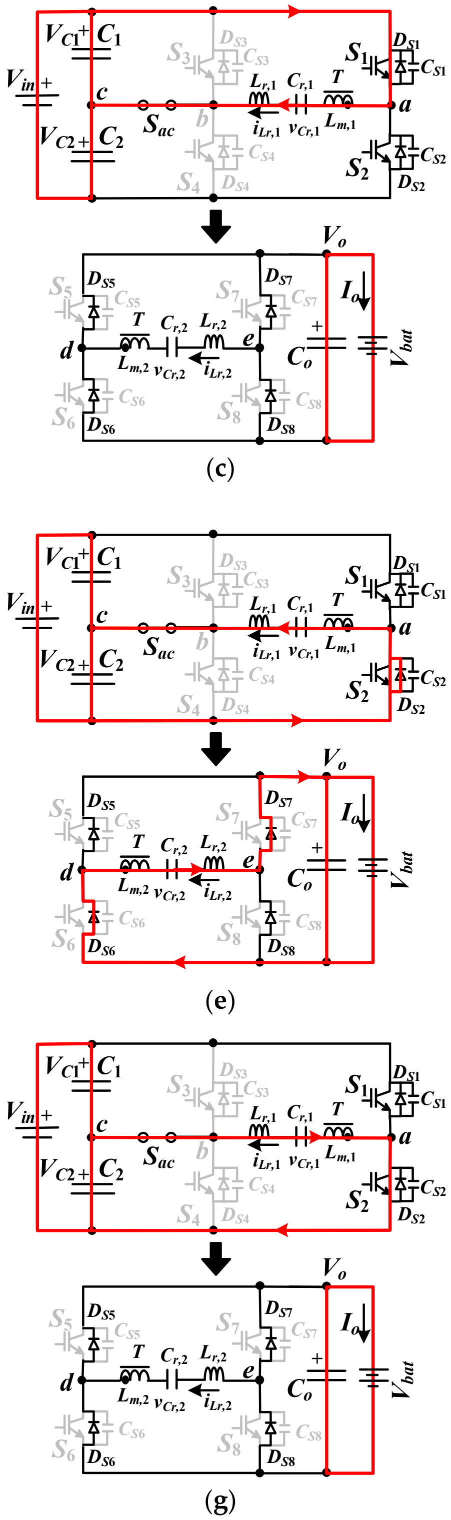

Figure 5. Equivalent circuits under low-output voltage range and forward power operation: (**a**) state 1; (**b**) state 2; (**c**) state 3; (**d**) state 4; (**e**) state 5; (**f**) state 6; (**g**) state 7; (**h**) state 8.

3.2. High-Output Voltage Range under Forward Power Operation

When high-output voltage range is demanded in the proposed converter, the full bridge resonant converter is selected on the primary side to achieve high voltage gain. Therefore, S_{ac} is off and S_1–S_4 are controlled with frequency modulation to regulate the load voltage. Switches S_5–S_8 are off and the secondary side operates as a full bridge diode rectifier. Owing to the status of S_1–S_4 and D_{S5}–D_{S8}, eight switching states are operated in every switching cycle as shown in Figure 4b. The circuits of these eight switching states are provided in Figure 6. Since the full bridge resonant circuit in Figure 6 and half bridge resonant circuit in Figure 5 have the similar operation states with diffenent voltage gains, the state operations of the presented converter operated at high-output voltage range under forward power operation are neglected in this subsection.

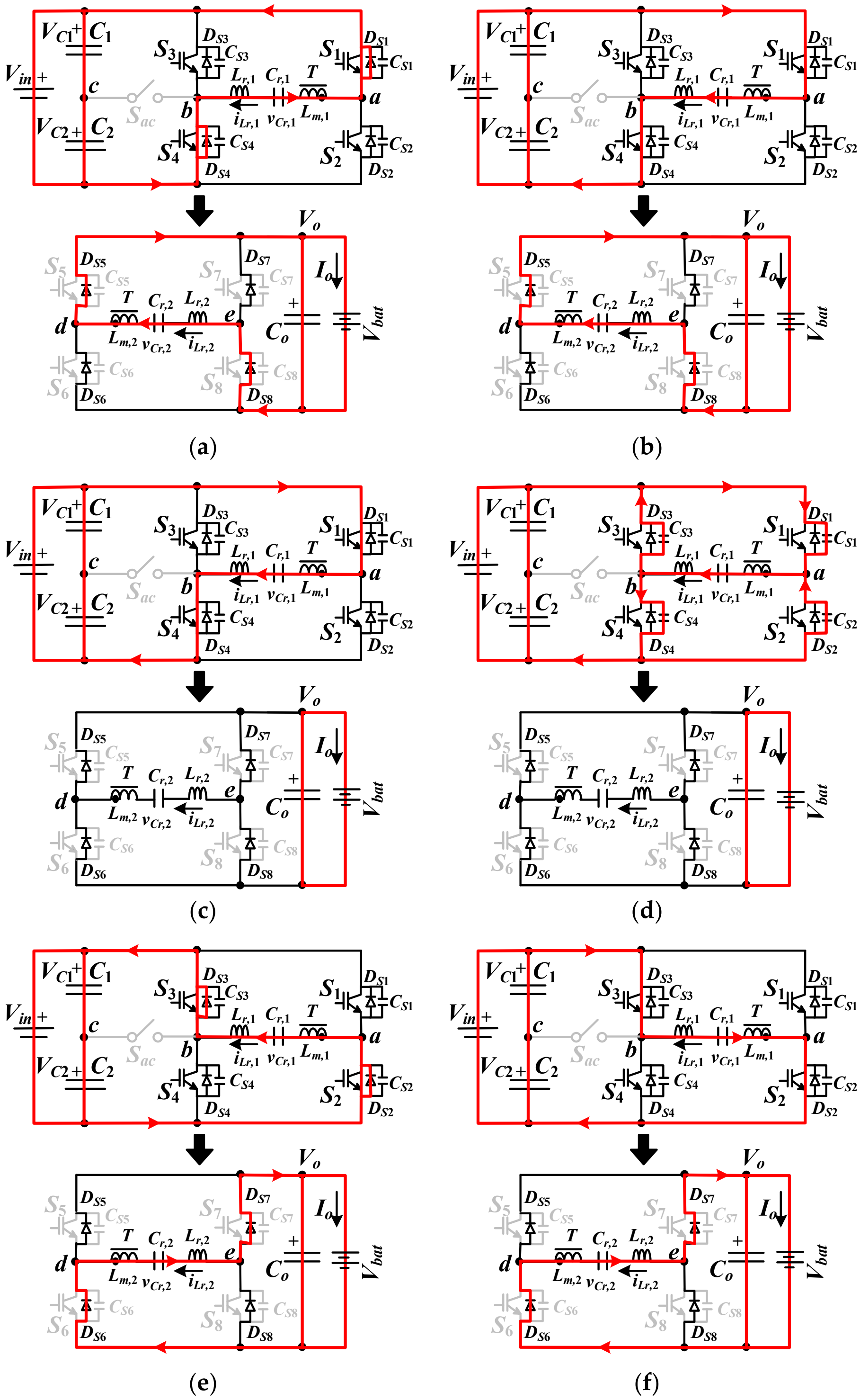

Figure 6. *Cont.*

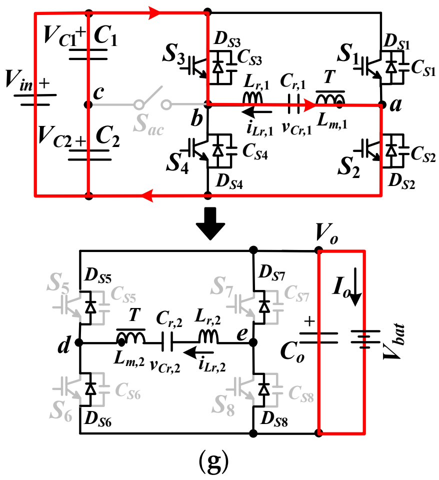

Figure 6. Equivalent circuits under high-output voltage range and forward power operation: (**a**) state 1; (**b**) state 2; (**c**) state 3; (**d**) state 4; (**e**) state 5; (**f**) state 6; (**g**) state 7; (**h**) state 8.

3.3. Under Backward Power Operation

When the presented converter is demanded to achieve backward power operation, the circuit operation under reverse power transfer from V_o to V_{in} is given in Figure 3d. Switch S_{ac} and S_1–S_4 are off and S_5–S_8 are controlled with frequency modulation. The full bridge diode rectifier and full bridge resonant circuit are operated on the left and right hand sides, respectively, of the presented circuit. Based on status of S_5–S_8 and D_{S1}–D_{S4}, the proposed converter operated in Figure 3d has eight switching states (Figure 4c) in every switching cycle. Figure 7 provides eight state circuits under backward power operation.

State 1 [t_0, t_1]: At time t_0, $v_{CS5} = v_{CS8} = 0$. Owing to $i_{Lr,2}(t_0) < 0$, D_{S5} anf D_{S8} are conducting. S_5 and S_8 turn on at this moment to accomplish zero voltage switching. On the left hand side, $i_{Lr,1} > 0$ and D_{S1} and D_{S4} are conducting.
State 2 [t_1, t_2]: At time t_1, $i_{Lr,2}$ becomes positive and D_{S5} and D_{S8} are off. Therefore, the positive current $i_{Lr,2}$ flows through S_5 and S_8. Power is transferred from V_o to V_{in} in this state. The leg voltages are $V_{ab} = V_{in}$ and $V_{de} = V_o$. In state 2, the resonant frequency is $f_r = 1/(2\pi\sqrt{L_{r,2}C_{r,2}})$.
State 3 [t_2, t_3]: If $f_r > f_{sw}$, the current $i_{Lr,1}$ will be decreased to 0 at time t_2. Then, D_{S1} and D_{S4} become off. The resonant frequency in state 3 is expressed as $f_p = 1/(2\pi\sqrt{C_{r,2}(L_{m,2} + L_{r,2})})$.
State 4 [t_3, t_4]: At time t_3, S_5 and S_8 are turned off. The current $i_{Lr,2}$ discharge C_{S6} and C_{S7}. If the current $i_{Lr,2}(t_3) = i_{Lm,2,peak} > V_o\sqrt{2C_{S,2}/L_{r,2}}$ where $i_{Lm,2,peak}$ is the peak value of $i_{Lm,2}$ and $C_{S,2} = C_{S5} = C_{S6} = C_{S7} = C_{S8}$, then C_{S6} and C_{S7} are discharged to zero voltage.
State 5 [t_4, t_5]: At time t_4, $v_{CS6} = v_{CS7} = 0$. Owing to $i_{Lr,2}(t_4) > 0$, D_{S6} and D_{S7} are conducting. S_6 and S_7 turn on at this moment to realize zero voltage switching. The current $i_{Lr,1}(t) < 0$ and D_{S2} and D_{S3} are conducting.
State 6 [t_5, t_6]: At time t_5, $i_{Lr,2}$ becomes negative and D_{S6} and D_{S7} are off. The current $i_{Lr,2}$ flows through S_6 and S_7. Power is transferred from V_o to V_{in} in state 6.
State 7 [t_6, t_7]: At time t_6, $i_{Lr,1} = 0$ so that D_{S2} and D_{S3} are off. The resonant frequency in state 7 is $f_p = 1/(2\pi\sqrt{C_{r,2}(L_{m,2} + L_{r,2})})$.
State 8 [t_7, $T_{sw} + t_0$]: At time t_7, S_6 and S_7 are off. The current $i_{Lr,2}$ discharges C_{S5} and C_{S8}. This switching cycle is ended at time $T_{sw} + t_0$ when $v_{CS5} = v_{CS8} = 0$.

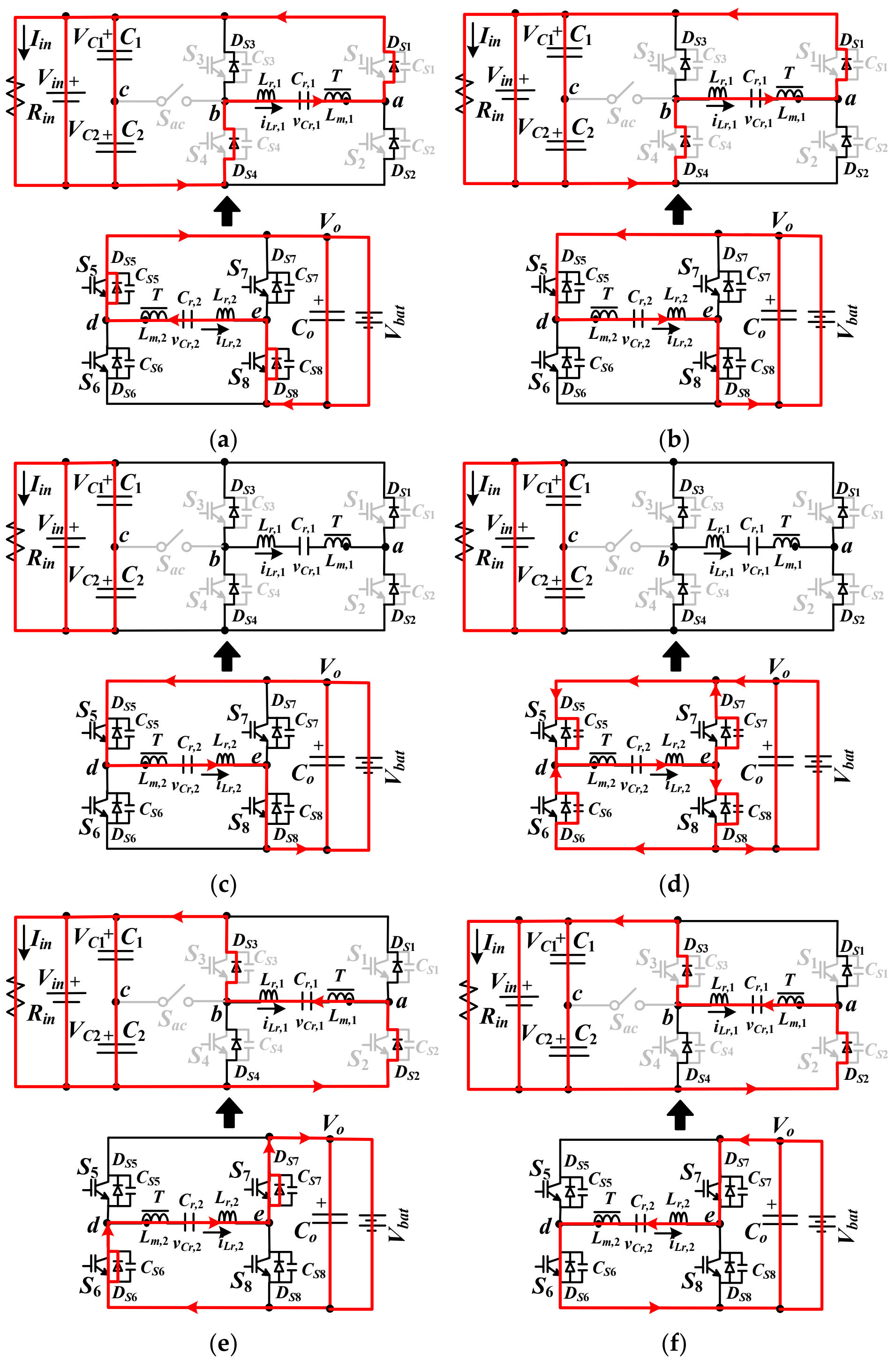

Figure 7. *Cont.*

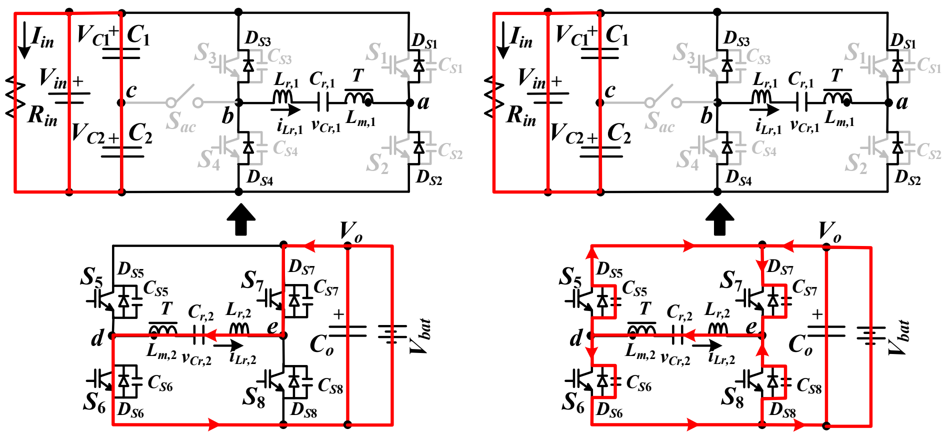

(g) (h)

Figure 7. Equivalent circuits under backward power operation: (**a**) state 1; (**b**) state 2; (**c**) state 3; (**d**) state 4; (**e**) state 5; (**f**) state 6; (**g**) state 7; (**h**) state 8.

4. Circuit Analysis and Design Procedures

The presented converter has three operation modes: forward power operation with low-output voltage range, forward power operation with high-output voltage range, and backward power operation as shown in Figures 3–6. The frequency modulation is selected to control active devices and regulate load voltage. Therefore, the voltage gain of the presented converter is related to the switching frequency. The equivalent resonant circuits based on the fundamental switching frequency analysis are shown in Figure 8 for three operation modes. For low- and high-output voltage range modes under forward power operation, the input terminal voltages are $V_{ac} = \pm V_{in}/2$ and $V_{ab} = \pm V_{in}$, respectively. The root-mean-square leg voltages are expressed as $V_{ac,F} = \sqrt{2}V_{in}/\pi$ and $V_{ab,F} = 2\sqrt{2}V_{in}/\pi$. The equivalent load resistance $R_{o,ac}$ at fundamental switching frequency under forward power operation is given as $R_{o,ac} = 8n^2R_o/\pi^2$. For backward power operation, the leg voltage $V_{de} = \pm V_o$ and the equivalent resistance $R_{in,ac}$ at fundamental switching frequency is expressed as $R_{in,ac} = 8R_{in}/(\pi^2n^2)$. Similarly, the fundamental leg voltage $V_{de,F} = 2\sqrt{2}V_o/\pi$.

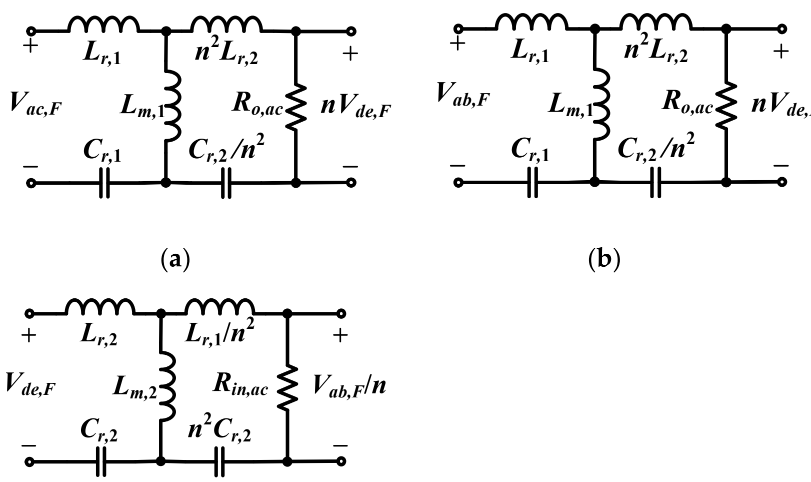

(a) (b) (c)

Figure 8. The equivalent resonant circuits at fundamental switching frequency under (**a**) low-output voltage range and forward power operation; (**b**) high-output voltage range and forward power operation; (**c**) backward power operation.

In Figure 8, the voltage transfer functions under three operation modes can be derived in Equations (1)–(3).

$$M_{ac,F,Low}(s) = \frac{nV_{de,F}}{V_{ac,F}} = \frac{2\sqrt{2}nV_o/\pi}{\sqrt{2}V_{in}/\pi} = \frac{sL_{m,1}//\left(sn^2L_{r,2}+\frac{n^2}{sC_{r,2}}+R_{o,ac}\right)}{sL_{r,1}+\frac{1}{sC_{r,1}}+\left[sL_{m,1}//\left(sn^2L_{r,2}+\frac{n^2}{sC_{r,2}}+R_{o,ac}\right)\right]} \times \frac{R_{o,ac}}{sn^2L_{r,2}+\frac{n^2}{sC_{r,2}}+R_{o,ac}} \quad (1)$$

$$M_{ac,F,High}(s) = \frac{nV_{de,F}}{V_{ab,F}} = \frac{2\sqrt{2}nV_o/\pi}{2\sqrt{2}V_{in}/\pi} = \frac{sL_{m,1}//\left(sn^2L_{r,2}+\frac{n^2}{sC_{r,2}}+R_{o,ac}\right)}{sL_{r,1}+\frac{1}{sC_{r,1}}+\left[sL_{m,1}//\left(sn^2L_{r,2}+\frac{n^2}{sC_{r,2}}+R_{o,ac}\right)\right]} \times \frac{R_{o,ac}}{sn^2L_{r,2}+\frac{n^2}{sC_{r,2}}+R_{o,ac}} \quad (2)$$

$$M_{ac,B}(s) = \frac{nV_{ab,F}/n}{V_{de,F}} = \frac{2\sqrt{2}V_{in}/(n\pi)}{2\sqrt{2}V_o/\pi} = \frac{sL_{m,2}//\left(sL_{r,1}/n^2+\frac{1}{sn^2C_{r,1}}+R_{in,ac}\right)}{sL_{r,2}+\frac{1}{sC_{r,2}}+\left[sL_{m,2}//\left(sL_{r,1}/n^2+\frac{1}{sn^2C_{r,1}}+R_{in,ac}\right)\right]} \times \frac{R_{in,ac}}{sL_{r,1}/n^2+\frac{1}{sn^2C_{r,1}}+R_{in,ac}} \quad (3)$$

If the following parameters are defined as $Q = \sqrt{L_{r,1}/C_{r,1}}/R_{o,ac}$, $Q' = \sqrt{L_{r,2}/C_{r,2}}/R_{in,ac}$, $K = L_{m,1}/L_{r,1}$, $K' = L_{m,2}/L_{r,2} = K$, and $F = F' = f_{sw}/f_r$, then Equations (1)–(3) can be rewritten in Equations (4)–(6) for forward power operation under low-output voltage range, forward power operation under high-output voltage range, and backward power operation, respectively.

$$|M_{ac,F,Low}(Q,F,K)| = \frac{2nV_o}{V_{in}} = \frac{1}{\sqrt{[1+\frac{1}{K}-\frac{1}{KF^2}]^2+Q^2[F(2+\frac{1}{K})-\frac{1}{F}(2+\frac{2}{K}-\frac{1}{KF^2})]^2}} \quad (4)$$

$$\left|M_{ac,F,High}(Q,F,K)\right| = \frac{nV_o}{V_{in}} = \frac{1}{\sqrt{[1+\frac{1}{K}-\frac{1}{KF^2}]^2+Q^2[F(2+\frac{1}{K})-\frac{1}{F}(2+\frac{2}{K}-\frac{1}{KF^2})]^2}} \quad (5)$$

$$|M_{ac,B}(Q',F',K')| = \frac{V_{in}}{nV_o} = \frac{1}{\sqrt{[1+\frac{1}{K'}-\frac{1}{K'F'^2}]^2+Q'^2[F'(2+\frac{1}{K'})-\frac{1}{F'}(2+\frac{2}{K'}-\frac{1}{K'F'^2})]^2}} \quad (6)$$

One can observe that the voltage transfer functions in Equations (4)–(6) are similar. Figure 9a gives the voltage transfer function under K = 5.

The design procedures of the presented converter are provided in this section to obtain the circuit components in the laboratory prototype. The input voltage V_{in} = 400 V, the output battery voltage V_o = 200–450 V, the rated power $P_{o,rated}$ = 1 kW, the rated load current $I_{o,rated}$ = 2.3 A, and the resonant frequency f_r = 70 kHz. The constant current or constant voltage is selected to charge the battery stack. If the battery stack voltage is in a low voltage range V_o = 200–310 V, the half bridge resonant circuit (S_{ac} on; S_3 and S_4 off) is operated on the left hand side of the converter. If the output battery stack voltage is in the high voltage range V_o = 310–450 V, the full bridge resonant circuit (S_{ac} off) is operated on the proposed converter to achieve battery charge (forward power operation). For backword power operation (battery discharge from V_o to V_{in}), the load voltage (V_{in}) is regulated at 400 V. Since the voltage transfer functions in (4)–(6) have the same circuit characteristics for both forward and backward power operations, the circuit components of the presented converter are derived from forward power operation and low-output voltage range (V_o = 200–310 V). In Equation (4), the voltage gain is related to the output voltage. The high-output voltage will result in large dc voltage gain. In this design example, the assumed minimum voltage gain $|M_{ac,F,Low}|_{min}$ = 1 at $V_{o,min}$ = 400 V and V_o = 200 V. From Equation (4), the transformer turns ratio n can be expressed in Equation (7).

$$n = |M_{ac,F,Low}|_{\min} \times \frac{V_{in}}{2V_{o,\min}} = 1 \times \frac{400}{2 \times 200} = 1 \quad (7)$$

In this prototype circuit, the selected primary windings (N_p) are 90 turns and secondary windings (N_s) are 90 turns. The transformer T is implemented with magnetic core PC40/EE40. According to the selected turn ratio n, the maximum voltage gain in Equation (4) can be obtained as.

$$|G_{ac,F,Low}|_{\max} = \frac{2nV_{o,\max}}{V_{in}} = \frac{2 \times 1 \times 310}{400} = 1.55 \tag{8}$$

Figure 9b illustrates gain curves under K = 5 condition. From the given minimum and maximum dc voltage gains, one can observe the voltage gain $|M_{ac,F,Low}|$ curves under quality factor Q < 0.3 are greater than 1.55. That means the corresponding switching frequency index F can be obtained from $V_{o,min}$ = 200 V to $V_{o,max}$ = 310 V to control load voltage. Therefore, Q = 0.3 is used in this design example to obtain the other circuit components. $R_{o,ac}$ at full load can be derived in Equation (9).

$$R_{o,ac} = \frac{8n^2R_o}{\pi^2} = \frac{8 \times 1^2 \times (310^2/1000)}{3.14159^2} \approx 78\Omega \tag{9}$$

From the given Q and $R_{o,ac}$, the primary passive components are derived in Equations (10)–(12).

$$C_{r,1} = \frac{1}{2\pi Q f_r R_{o,ac}} = \frac{1}{2 \times 3.14159 \times 0.3 \times 70000 \times 78} \approx 97 \text{ nF} \tag{10}$$

$$L_{r,1} = \frac{QR_{o,ac}}{2\pi f_r} = \frac{0.3 \times 78}{2 \times 3.14159 \times 70000} \approx 53 \text{ μH} \tag{11}$$

$$L_{m,1} = KL_{r,1} = 5 \times 53 = 265 \text{ μH} \tag{12}$$

Then, the secondary resonant components of the proposed converter are obtained as:

$$C_{r,2} = n^2C_{r,1} = 97 \text{ nF} \tag{13}$$

$$L_{r,2} = L_{r,1}/n^2 = 53 \text{ μH} \tag{14}$$

The resonant inductors $L_{r,1}$ and $L_{r,2}$ are implemented with magnetic cores PC40/EER35. Power switches FGH60N60UFD with 600 V/60 A rating are used for switches S_1–S_8. Power switch 6R125P6 with 650 V/19 A rating is used for switch S_{ac}. The input and output capacitances are C_1 = C_2 = 2.2 μF/630 V and C_o = 660 μF/800 V.

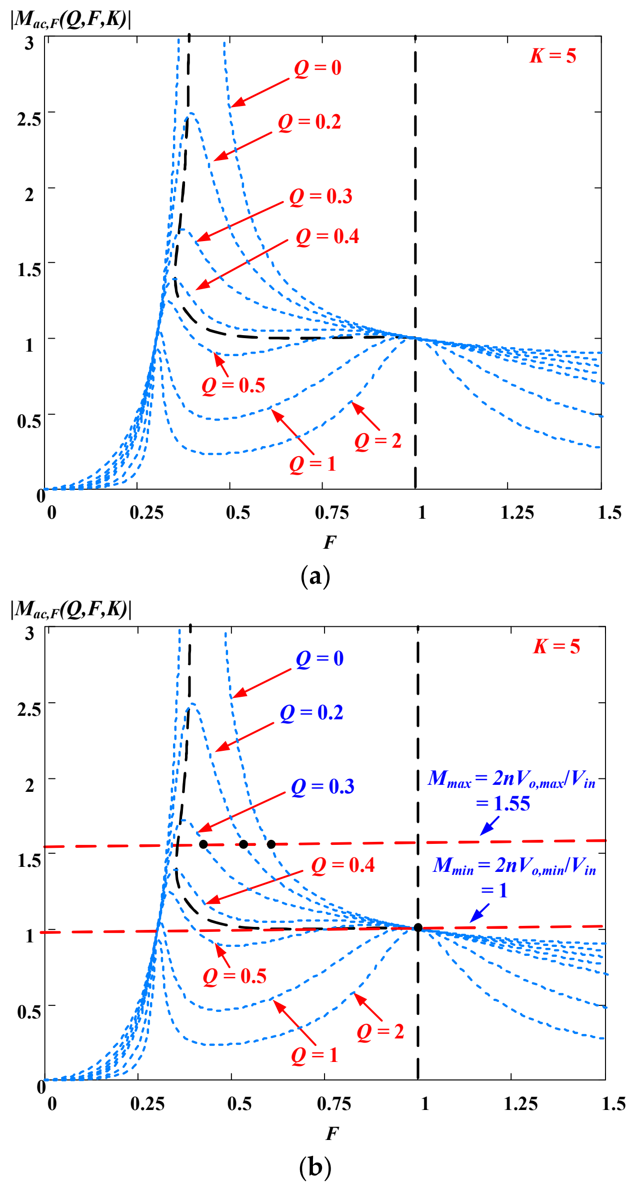

Figure 9. Gain curves: (**a**) the proposed converter (**b**) in the laboratory prototype.

5. Experimental Results

Figure 10a gives the measured load voltage (battery voltage) and load current (battery current). For battery charge, the constant current mode (CC mode) I_o = 2.3 A is used to charge the load voltage (battery voltage) from 200 V to 450 V. Then, the constant voltage mode (CV mode) V_o = 450 V is used to charge the battery stack (load) so that the load current is decreased from the rated load current I_o = 2.3 A. The measured load voltage V_o = 200 V to 450 V and switch signals v_{Sac} and v_{S3} are given in Figure 10b. When 200 V < V_o < 310 V, S_{ac} is on and S_3 is off (half bridge resonant circuit). On the other hand, S_{ac} is off and S_3 is triggered by frequency control (full bridge resonant circuit) when 450 V > V_o > 310 V. Figures 11–14 give the experimental waveforms of the proposed converter operated at forward power flow. Figure 15 shows the measured waveforms of the proposed converter operated at backward power flow. Figure 11 shows the measured waveforms of the proposed converter operated at V_o = 200 V and the rated load current I_o = 2.3 A. Figure 11a gives the measured input voltage, output voltage, and load current. Since the half bridge resonant circuit is operated under V_o = 200 V, the switches S_3 and S_4 are off and S_{ac} is on. S_1 and S_2 are controlled with frequency modulation. The measured switch signals of S_1 and S_2 and the resonant waveforms v_{Cr1} and i_{Lr1} on the primary side are given in Figure 11b. Since the voltage gain of the converter at V_o = 200 V is unity, the switching frequency is close to the resonant frequency. Therefore, the resonant current waveform i_{Lr1} approximates a sinusoidal signal. The measured v_{Cr2}, i_{Lr2}, i_{DS5}, and i_{DS7} on the secondary side are provided in Figure 11c. Figure 11d gives the switch voltage and current of S_1. One can observe that S_1 is turned on at zero voltage so that the turn-on switching loss is eliminated. Figure 12 gives the experimental results of the proposed converter operated at half bridge resonant mode (Figure 3b) under V_o = 310 V and the rated current I_o = 2.3 A with constant current mode control. Since the converter has higher voltage gain at V_o = 310 V, the switching frequency is less than the resonant frequency, as shown in Figure 9b. The primary resonant current i_{Lr1} approximates a quasi-sinusoidal waveform (Figure 12b). In Figure 12c, the voltage v_{Cr2} is constant during i_{Lr2} = 0 because no current flows through C_{r2}. The diodes D_{S5} and D_{S7} are turned off at zero current switching. In Figure 12d, S_1 is turned on at zero voltage switching. In Figures 13 and 14, the proposed converter is operated at the full bridge resonant circuit (Figure 3c) under V_o = 450 V and I_o = 2.3 A and 1.15 A, respectively, with constant voltage mode control. Figures 13b and 14b show the switching signals of S_1–S_4 under 100% and 50% rated load current. Figures 13c and 14c give the measured leg voltage v_{ab} and resonant waveforms v_{Cr1} and i_{Lr1} on the primary side for 100% and 50% rated load current. Similarly, the measured resonant waveforms and diode currents on the secondary side are provided in Figures 13d and 14d. The diodes D_{S5} and D_{S7} are turned off at zero current switching. In Figures 13e and 14e, one can observe that S_1 is turned on at zero voltage switching for both 100% and 50% rated load current. Figure 15 gives the measured waveforms of the proposed converter operated at backward power operation from V_o = 450 V to V_{in} = 400 V. Under backward power operation, all switches on the primary side are off and S_5–S_8 are controlled with frequency modulation. Figure 15a gives the experimental waveforms of V_o, V_{in}, and I_{in} at full power condition. Figure 15b shows the switching signals of S_5–S_8. The leg voltage v_{de} and resonant waveforms v_{Cr2} and i_{Lr2} on the secondary side are measured and provided in Figure 15c. The primary side resonant waveforms i_{Lr1} and v_{Cr1} and diode currents i_{DS1} and i_{DS3} are provided in Figure 15d. In Figure 15e, it is clear that S_5 is turned on at zero voltage switching. The measured efficiencies of the proposed converter are 92.3%, 93.5%, and 91.5% at V_o = 200 V, 310 V, and 450 V, respectively, under the rated load current with constant current mode control. Figure 16 gives a picture of the prototype circuit. The comparisons between the conventioal dual active bridge converter, *CLLC* converters, and the studied converter are provided in Table 1. It is clear that two more power switches and split capacitors are used in the proposed circuit. However, more wide output voltage can be operated in the studied circuuit.

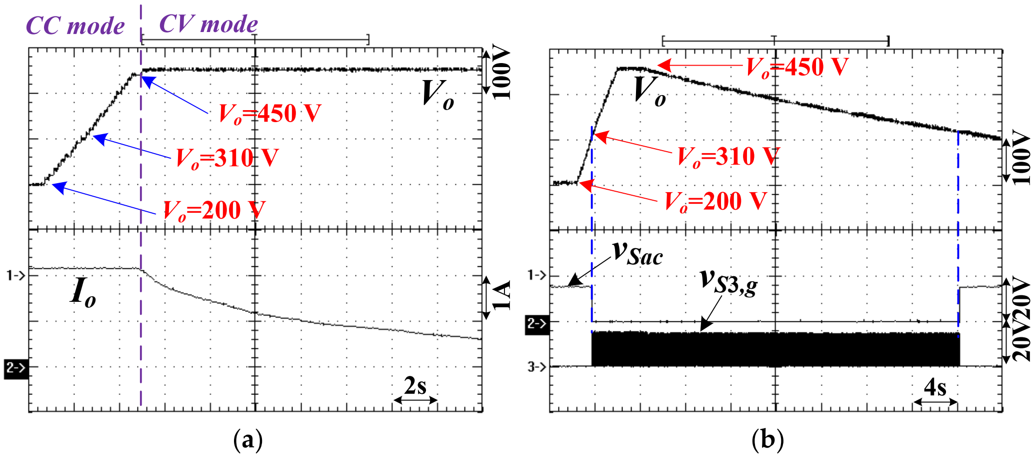

Figure 10. Measured waveforms (**a**) V_o and I_o under constant current (CC) mode and constant voltage (CV) mode control; (**b**) V_o, v_{Sac}, and $v_{S3,g}$.

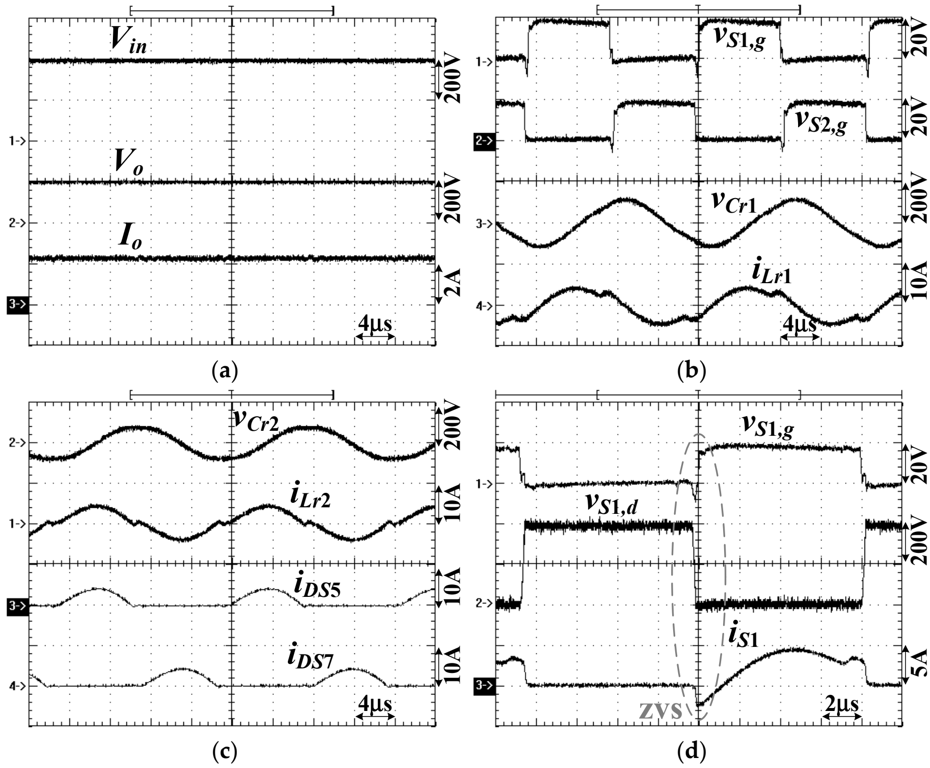

Figure 11. Experimental waveform of the proposed converter at V_o = 200 V and the rated load current (**a**) V_{in}, V_o, and I_o; (**b**) $v_{S1,g}$, $v_{S2,g}$, v_{Cr1}, and i_{Lr1}; (**c**) v_{Cr2}, i_{Lr2}, i_{DS5}, and i_{DS7}; (**d**) $v_{S1,g}$, $v_{S1,d}$, and i_{S1}.

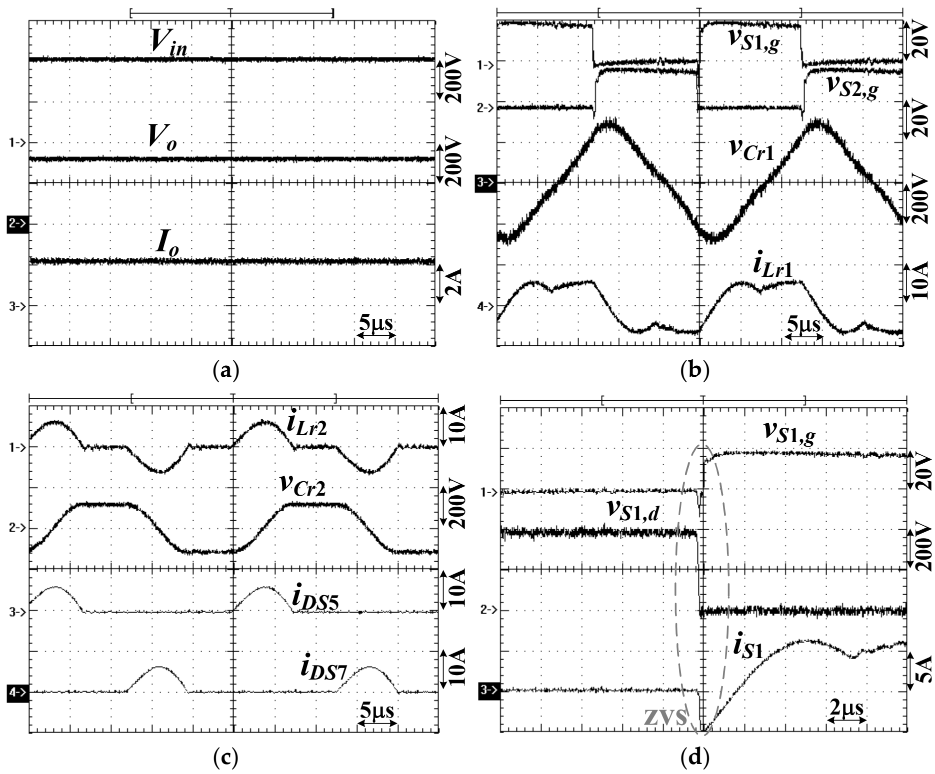

Figure 12. Experimental waveform of the proposed converter at V_o = 310 V and the rated load current (**a**) V_{in}, V_o, and I_o; (**b**) $v_{S1,g}$, $v_{S2,g}$, v_{Cr1}, and i_{Lr1}; (**c**) i_{Lr2}, v_{Cr2}, i_{DS5}, and i_{DS7}; (**d**) $v_{S1,g}$, $v_{S1,d}$, and i_{S1}.

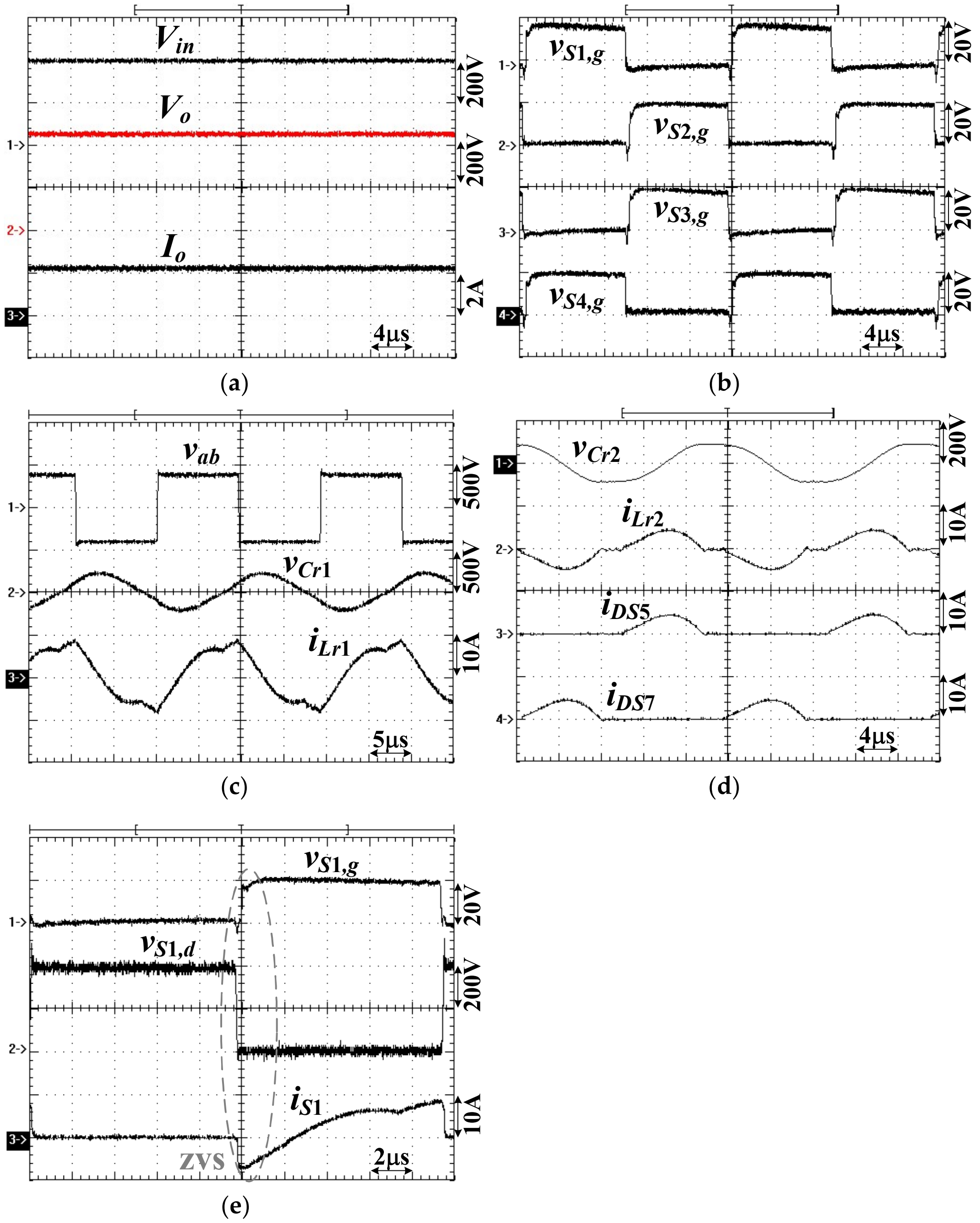

Figure 13. Experimental waveform of the proposed converter at V_o = 450 V and the rated load current (**a**) V_{in}, V_o, and I_o; (**b**) $v_{S1,g}$–$v_{S4,g}$; (**c**) v_{ab}, v_{Cr1}, and i_{Lr1}; (**d**) v_{Cr2}, i_{Lr2}, i_{DS5}, and i_{DS7}; (**e**) $v_{S1,g}$, $v_{S1,d}$; and i_{S1}.

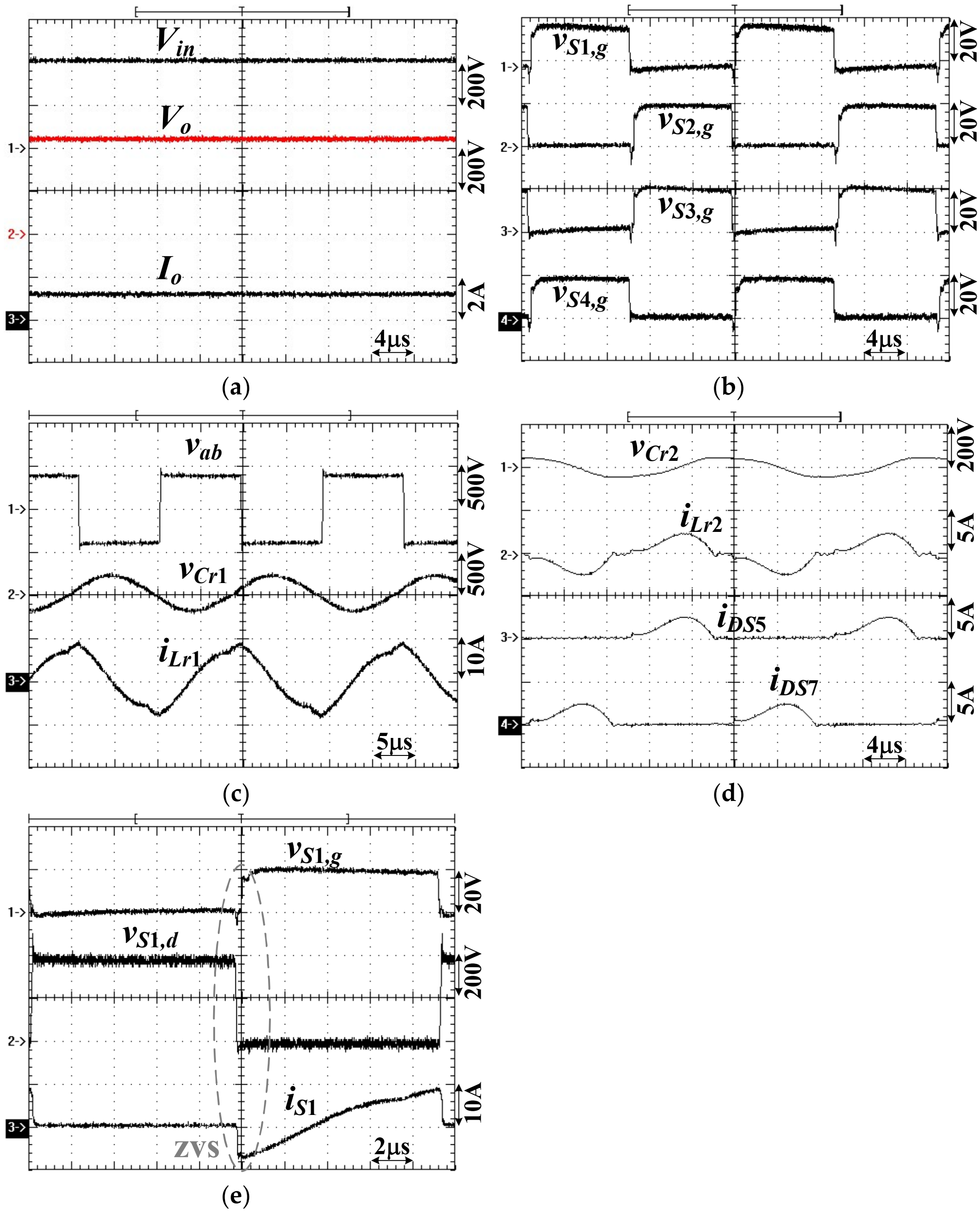

Figure 14. Experimental waveform of the proposed converter at V_o = 450 V and 50% rated load current (**a**) V_{in}, V_o, and I_o; (**b**) $v_{S1,g}$–$v_{S4,g}$; (**c**) v_{ab}, v_{Cr1}, and i_{Lr1}; (**d**) v_{Cr2}, i_{Lr2}, i_{DS5}; and i_{DS7}; (**e**) $v_{S1,g}$, $v_{S1,d}$; and i_{S1}.

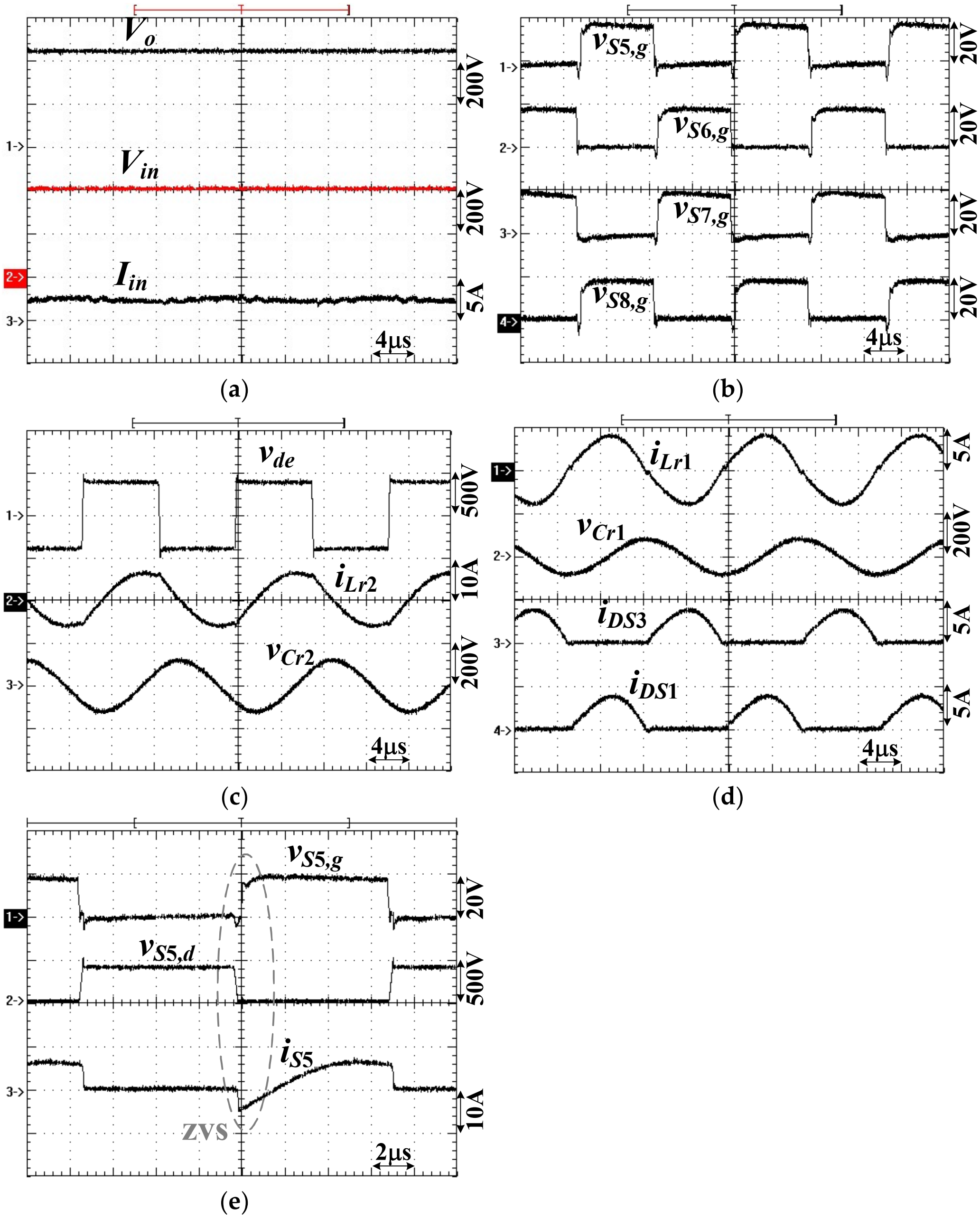

Figure 15. Experimental waveform of the proposed converter operated at backward power flow from V_o = 450 V to V_{in} = 400 V under the rated power condition (**a**) V_o, V_{in}, and I_{in}; (**b**) $v_{S5,g}$–$v_{S8,g}$; (**c**) v_{de}, i_{Lr2}, and v_{Cr2}; (**d**) i_{Lr1}, v_{Cr1}, i_{DS3}, and i_{DS1}; (**e**) $v_{S5,g}$, $v_{S5,d}$, and i_{S5}.

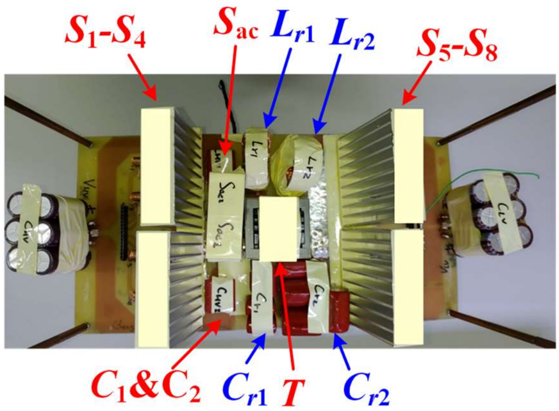

Figure 16. Picture of the prototype circuit.

Table 1. Comparisons between DAB converter, CLLC converter, and the studied converter.

Topology	Power Switches	Split Capacitor	Resonant Components	Voltage Range, Power Rating
DAB converter	8	0	1	V_{in} = 600 V, V_o = 300–450 V, P_o = 10 kW in [11]
Dual half bridge CLLC converter	4	4	4	V_{in} = 400–600 V, V_o = 300–450 V, P_o = 3.3 kW in [15]
Dual full bridge CLLC converter	8	0	4	V_{in} = 382–408 V, V_o = 50 V, P_o = 400 W in [16]
Proposed converter	10	2	4	V_{in} = 400 V, V_o = 200–450 V, P_o = 1 kW

6. Conclusions

A bidirectional resonant converter is proposed, analyzed, and implemented for wide voltage range battery charger/discharger applications. The proposed converter can be used between the DC microgrid system and the electric vehicle charge station to realize G2V charge and V2G discharge operations. The proposed converter has symmetric resonant circuits on the primary and secondary sides to realize bidirectional power flow control. By selecting the half bridge or full bridge circuit structure operation, the proposed circuit can achieve low or high voltage gain. Therefore, the wide output voltage control can be implemented in the proposed converter to avoid wide switching frequency variation in conventional bidirectional resonant converters. Due to the resonant circuit behaviors, the power switches are turned on at zero voltage switching so that the switching loss can be reduced. The circuit operation principle, system analysis, circuit characteristics, and design example of the prototype circuit are provided in this paper. The experiments are also provided to validate the performance of the presented converter.

Funding: This research is supported by the National Yunlin University of Science and Technology, Taiwan, under grant number 109H500311.

Institutional Review Board Statement: Not applicable.

Informed Consent Statement: Not applicable.

Acknowledgments: The author thanks the financial support by the National Yunlin University of Science and Technology, Taiwan, under grant number 109H500311. The author would also like to thank Y.-C. Liu for his help to measure and validate the experimental waveforms.

Conflicts of Interest: The authors declare no conflict of interest.

References

1. Dragicevic, T.; Lu, X.; Vasquez, J.C.; Guerrero, J.M. DC microgrids—Part I: A review of control strategies and stabilization techniques. *IEEE Trans. Power Electron.* **2016**, *31*, 4876–4891. [CrossRef]
2. Dragicevic, T.; Lu, X.; Vasquez, J.C.; Guerrero, J.M. DC microgrids—Part II: A review of power architectures, applications, and standardization issue. *IEEE Trans. Power Electron.* **2016**, *31*, 3528–3549. [CrossRef]
3. Emadi, A.; Lee, Y.J.; Rajashekara, K. Power electronics and motor drives in electric, hybrid electric, and plug-in hybrid electric vehicles. *IEEE Trans. Ind. Electron.* **2008**, *55*, 2237–2245. [CrossRef]
4. Guerrero, J.M.; Loh, P.C.; Lee, T.L.; Chandorkar, M. Advanced control architectures for intelligent microgrids—Part II: Power quality, energy storage, and ac/dc microgrids. *IEEE Trans. Ind. Electron.* **2013**, *60*, 1263–1270. [CrossRef]
5. Meng, L.; Shafiee, Q.; Trecate, G.F.; Karimi, H.; Fulwani, D.; Lu, X.; Guerrero, J.M. Review on control of DC microgrids and multiple microgrid clusters. *IEEE J. Emerg. Sel. Top. Power Electron.* **2017**, *5*, 928–948.
6. Mangu, B.; Akshatha, S.; Suryanarayana, D.; Fernandes, B.G. Grid-connected PV-wind-battery-based multi-input transformer-couple bidirectional dc-dc converter for household applications. *IEEE J. Emerg. Sel. Top. Power Electron.* **2016**, *4*, 1086–1095. [CrossRef]
7. Yilmaz, M.; Krein, P.T. Review of battery charger topologies, charging power levels, and infrastructure for plug-in electric and hybrid vehicles. *IEEE Trans. Power Electron.* **2013**, *28*, 2151–2169. [CrossRef]
8. Ahrabi, R.R.; Ardi, H.; Elmi, M.; Ajami, A. A novel step-up multi input dc-dc converter for hybrid electric vehicles application. *IEEE Trans. Power Electron.* **2017**, *32*, 3549–3561. [CrossRef]
9. Xu, D.; Zhao, C.; Fan, H. A PWM plus phase-shift control bidirectional DC-DC converter. *IEEE Trans. Power Electron.* **2004**, *19*, 666–675. [CrossRef]
10. Tao, H.; Kotsopoulos, A.; Duarte, J.L.; Hendrix, M.A.M. Family of multiport bidirectional DC-DC converters. *IEE Proc. Electr. Power Appl.* **2006**, *153*, 451–458. [CrossRef]
11. Jain, A.K.; Ayyanar, R. PWM control of dual active bridge: Comprehensive analysis and experimental verification. *IEEE Trans. Power Electron.* **2011**, *26*, 1215–1227. [CrossRef]
12. Zhao, B.; Song, Q.; Liu, W.; Sun, Y. Overview of dual-active-bridge isolated bidirectional DC–DC converter for high-frequency-link power-conversion system. *IEEE Trans. Power Electron.* **2014**, *29*, 4091–4106. [CrossRef]
13. Rico, S.J.; Pagano, D.J.; Lucas, K.E. Bidirectional power sharing for DC microgrid enabled by dual active bridge DC-DC converter. *Energies* **2021**, *14*, 404.
14. Lara, J.; Masisi, L.; Hernandez, C.; Arjona, A.; Chandra, A. Novel five-level ANPC bidirectional converter for power quality enhancement during G2V/V2G operation of cascaded EV charger. *Energies* **2021**, *14*, 2650. [CrossRef]
15. Jung, J.H.; Kim, H.S.; Ryu, M.H.; Baek, J.W. Design methodology of bidirectional CLLC resonant converter for high-frequency isolation of DC distribution systems. *IEEE Trans. Power Electron.* **2013**, *28*, 1741–1755. [CrossRef]
16. Zou, S.; Lu, J.; Mallik, A.; Khaligh, A. Bi-directional CLLC converter with synchronous rectification for plug-in electric vehicles. *IEEE Trans. Ind. Appl.* **2018**, *54*, 998–1005. [CrossRef]
17. Lin, B.R. Analysis of a series-parallel resonant converter for DC microgrid applications. *Processes* **2021**, *9*, 542. [CrossRef]
18. Lin, B.R. Analysis and implementation of a frequency control DC-DC converter for light electric vehicle applications. *Electronics* **2021**, *10*, 1623. [CrossRef]